ACS OMEGA

Article

Cite This: ACS Omega 2019, 4, 2206−2216

http://pubs.acs.org/journal/acsodf

Highly Efficient Hybrid Ni/Nitrogenated Graphene Electrocatalysts for Hydrogen Evolution Reaction

Melisa J. Gómez, Antonella Loiácono, Luis A. Pérez, Esteban A. Franceschini,* and Gabriela I. Lacconi*

INFIQC-CONICET, Departamento de Fisicoquímica—Facultad de Ciencias Químicas, Universidad Nacional de Córdoba, Ciudad Universitaria, 5000 Córdoba, Argentina

ABSTRACT: Two nickel/nitrogenated graphene hybrid electrodes (**Ni-NrGO$_{NH3}$** and **Ni-NrGO$_{APTES}$**) were synthesized, and their catalytic activity with respect to the hydrogen evolution reaction (HER) in alkaline media was analyzed. Incorporation of nitrogen to the carbon structure in graphene oxide (GO) or reduced GO (rGO) flakes in aqueous solutions was carried out based on two different configurations. **NrGO$_{NH_3}$** particles were obtained by a hydrothermal method using ammonium hydroxide as the precursor, and **NGO$_{APTES}$** particles were obtained by silanization (APTES functionalization) of GO sheets. Aqueous dispersions containing **NrGO$_{NH_3}$** and **NGO$_{APTES}$** particles were added to the traditional nickel Watts plating bath in order to prepare the **Ni-NrGO$_{NH_3}$** and **Ni-NrGO$_{APTES}$** catalysts, respectively. Nickel substrates were coated with the hybrid nickel electrodeposits and used as electrodes for hydrogen production. The **Ni-NrGO** catalysts show a higher activity than the conventional nickel electrodeposited electrodes, particularly the ones containing APTES molecules because they allow obtaining a hydrogen current density 130% higher than conventional Ni-plated electrodes with a Watts bath in the absence of additives. In addition, both catalysts show a low deactivation rate during the ageing treatment, which is a sign of a longer midlife for the catalyst. Cyclic voltammetry and electrochemical impedance spectroscopy measurements were used for examination of the catalytic efficiency of hybrid **Ni-NrGO** electrodes for HER in KOH solution. High values of exchange current densities, 8.53×10^{-4} and 2.53×10^{-5} mA cm^{-2} for HER in alkaline solutions on **Ni-NrGO$_{NH_3}$** and **Ni-NrGO$_{APTES}$** electrodes, respectively, were obtained.

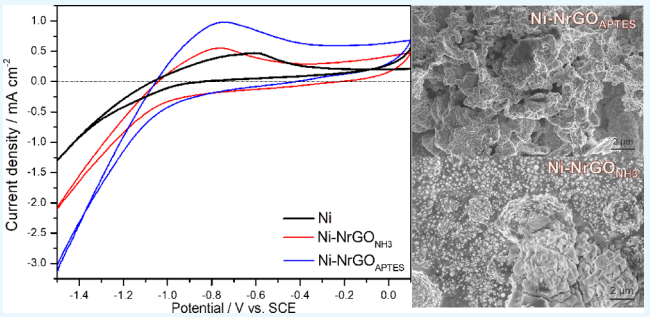

INTRODUCTION

The development of high activity electrocatalysts for the hydrogen evolution reaction (HER) is one of the main interests in renewable energy areas, particularly those that present high stability.[1,2] Moreover, nonexpensive and industrially scalable catalysts for alkaline electrolyser's electrodes obtained by simple methods are, nowadays, one of the technological topics most critical for systems useful for storage and conversion of energy.[3−5]

Electrolysis in alkaline medium is one of the most promising processes for both industrial and laboratory production of hydrogen because it allows the development of systems of various sizes, thus being a mature technology. Currently, conventional alkaline electrolysers use pure nickel electrodes which, although are economical compared to the catalysts for electrolysis in acid medium, have low catalytic activity and a high rate of activity loss,[6,7] constituting one of the main drawbacks for the application of this technology in the framework of hydrogen economy.

Graphene and its derivatives are the most studied nanomaterials of recent years because of their particular properties. Thus, when graphene oxide (GO) is reduced, the rapid mobility of charge carriers at room temperature reach values of 2×10^5 cm^2 V^{-1} s^{-1}, with an exceptional conductivity (10^6 S cm^{-1}), large theoretical specific surface area (2630 m^2 g^{-1}), and excellent optical transmittance (~97.7%).[8] These outstanding properties indicate that the reduced GO (rGO) can have great potential as a component in the construction of hybrid electrodes for various applications.[9] Production of rGO flakes has a significantly lower cost than the graphene thin films, being a nanomaterial with properties similar to those of graphene, such as high electrical conductivity, a very important characteristic when it is used as a component of the electrocatalysts.[10−12]

A promising strategy for tuning the electronic properties of graphene and its derivatives is doping them with heteroatoms. This type of chemical doping has been proved effective in carbon nanotubes with successful achievements to expand its applications.[13−16] The inclusion of N atoms into the graphene structure allows its transformation into p- or n-type semiconductors,[17] and three common bonding configurations with the carbon network can be observed: graphitic-N, pyridinic-N,

Received: October 21, 2018
Accepted: January 11, 2019
Published: January 29, 2019

DOI: 10.1021/acsomega.8b02895
ACS Omega 2019, 4, 2206−2216

and pyrrolic-N doped graphene[18] It has been proposed that pyridinic-N bonds usually contribute one p electron to the π system (sp^2), pyrrolic-N contributes two p electrons to the π system (sp^3), and graphitic N (normally denoted as quaternary N) is the N atoms that substitute C atoms in the hexagonal ring of the graphene structure (sp^2).[19] Different methods for obtaining nitrogenated graphene were proposed. The most common method involves modifications using hydrothermal processes.[20] Also, the functionalization with 3-aminopropyltriethoxysilane (APTES) molecules has been widely proven, where the amine groups interact with the oxygen functionalities on GO sheets.[21,22] It was also reported that composite catalysts formed with nickel nanoparticles supported on nitrogen-doped carbon nanotubes or nitrogen-doped graphene present enhanced catalytic activity for hydrogen oxidation reaction, and this feature comes from the synergetic effect of the combined structure.[23]

In the present paper, we have successfully prepared two kinds of stable nickel/nitrogenated-graphene hybrid electrodes, with different structural characteristics through nickel electrodeposition on nickel substrates. Evaluation of the electrocatalytic performance of nickel electrodes for HER in alkaline solutions is strongly improved by the incorporation of nitrogen-functionalized GO flakes, in the nickel matrix, changing the reactivity of the samples. The specific surface area and the inclusion of NGO particles conduce to an enhanced HER current. Moreover, the method used for hybrid catalysts is industrially scalable, and it allows its application in real alkaline electrolysis systems.

RESULTS AND DISCUSSION

N-graphene, **NrGO$_{NH_3}$**, and **NGO$_{APTES}$** particles were obtained by a hydrothermal process and silanization with APTES molecules, as detailed in the Experimental Section, and aqueous dispersions were obtained with both types of particles.

The electrocatalysts were obtained by plating nickel electrodes using a conventional Watts bath containing modified **N-GO** particles as additives. Electrodeposition of 30 μm thickness nickel films were obtained by a galvanostatic pulse (-0.05 A cm^{-2}) during 1800 s. The uniform approximation of all species in solution toward the electrode/solution interface was facilitated by controlled rotation of the electrode. During the electrodeposition, the potential reaches -5.0 V with both additives in the plating bath, at which the codeposited GO flakes were electrochemically reduced to rGO species. Therefore, we have considered that these included species in the nickel matrix are highly conductive. After the synthesis, **Ni-NrGO$_{NH_3}$** and **Ni-NrGO$_{APTES}$** electrodes were ready to evaluate their electrocatalytic activity for the HER.

Structural Characterization of Freshly Synthetized Electrodes. Figure 1 shows the scanning electron microscopy (SEM) micrographs of both types of synthesized electrodes. In the **Ni-NrGO$_{APTES}$** images (Figure 1A,B), a highly porous structure is observed, where the presence of some GO flakes can be evidenced between the electrodeposited nickel structures, forming a network with a high surface area. These types of surface structures are optimal for the proper functionality required for the electrocatalyst. **Ni-NrGO$_{NH_3}$** electrodes (Figure 1C,D) present a lobular surface with high roughness. Nickel electrodeposits in the presence of both

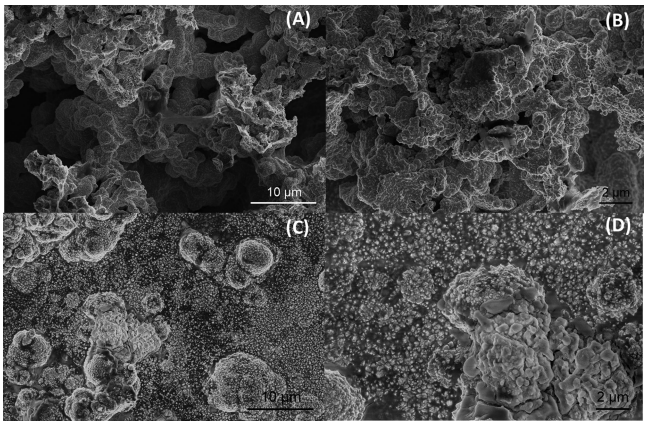

Figure 1. SEM micrograph of (A,B) **Ni-NrGO$_{APTES}$** at two different magnifications and (C,D) **Ni-NrGO$_{NH_3}$** at two different magnifications. All the images were obtained at 5 keV.

NGO particles are very different to those obtained in the absence of additives.[24]

Comparison of roughness from different nickel electrodeposits through the root mean square (rms) between peaks and valleys of confocal microscopy image profiles (not shown) is one important factor to establish the quality of catalyzers. Thus, **Ni-NrGO$_{APTES}$** electrodes have rms values approximately ten times higher than conventional Ni electrodeposits, whereas **Ni-NrGO$_{NH_3}$** electrodes are only seven times more rough (Table 1).

X-ray diffractograms of both synthesized electrodes, compared with a pure Ni electrodeposited sample are shown in Figure 2. Characteristic reflection peaks for crystalline nickel with a face-centered cubic (fcc) structure are clearly present for all samples. The 2θ values for the Ni(111) and (200) planes are presented in Table 1, together with the corresponding d-spacing distance and half peak widths (fwhm). Furthermore, data from **Ni-rGO** catalysts are included in Table 1, in order to analyze the structural changes that nitrogenated GO can enter the crystalline surface, in comparison with the pristine rGO.[24] Incorporation of **NrGO** and rGO flakes in the nickel matrix clearly produces a diminution in the fwhm, a feature that is usually associated with an increase of the crystal size. It can be observed that this effect is more pronounced for nitrogen-functionalized GO containing electrodes.

It has been found in the literature that graphene flakes serve as heterogeneous nucleation sites for grain growth during the electrodeposition process. This behavior has been attributed to the hybridization between p-orbital of graphene and d-orbital of Ni,[25] which improves the nucleation rate modifying the size of crystallites.[26]

On the other hand, the formation of (111) planes in the nickel film is always favored during the electrodeposition process because they are the most stable crystalline planes. However, the incorporation of **NrGO** in the Ni matrix produces a slight decrease of the (111)/(200) ratio as it can be seen in Table 1. In Figure 2, a shift from diffraction peaks to higher angle values with respect to the pure nickel electrode can be seen. It means that the d-spacing decreases for the **Ni-NrGO** electrodes; however, this change is barely noticeable (around 0.01 Å).

Characterization of the structure and electronic properties of carbon-derived materials is usually performed through Raman

DOI: 10.1021/acsomega.8b02895
ACS Omega 2019, 4, 2206−2216

Table 1. rms Values from Confocal Microscopy Images and X-ray Diffraction Parameters for Ni, Ni-rGO, Ni-NrGO$_{APTES}$, and Ni-NrGO$_{NH_3}$ Electrodeposited Catalysts[a]

electrode	rms (μm)	2θ		fwhm		d (Å)		crystal size (nm)		
plane		(111)	(200)	(111)	(200)	(111)	(200)	(111)	(200)	(111)/(200) ratio
Ni	0.43	44.49	51.75	0.216	0.354	2.04	1.77	39.1	24.1	19.36
Ni-rGO		44.56	51.95	0.153	0.256	2.03	1.76	55.3	33.3	31.80
Ni-NrGO$_{APTES}$	5.79	44.49	51.82	0.128	0.205	2.04	1.76	66.2	41.6	16.86
Ni-NrGO$_{NH_3}$	3.05	44.63	51.91	0.128	0.179	2.03	1.76	66.2	47.6	14.71

[a]Peak position (2θ), full-width at half maximum (fwhm), d-spacing, crystal size, and ratio between crystal planes for each signal of the synthesized catalysts.

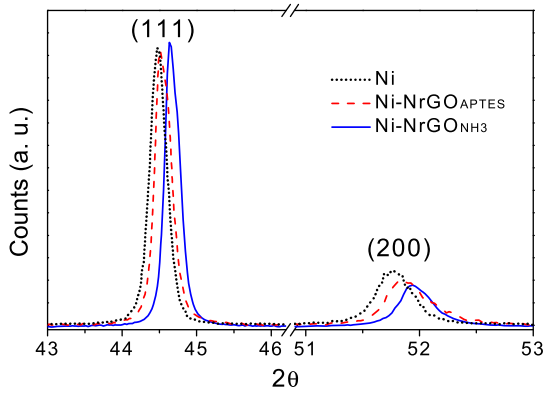

Figure 2. X-ray diffraction pattern of Ni, **Ni-NrGO$_{APTES}$**, and **Ni-NrGO$_{NH_3}$** catalysts.

spectroscopy analysis. The spectra of freshly synthesized catalysts (**Ni-NrGO$_{APTES}$** and **Ni-NrGO$_{NH_3}$**) are presented in Figure 3, together with the spectra of different graphene

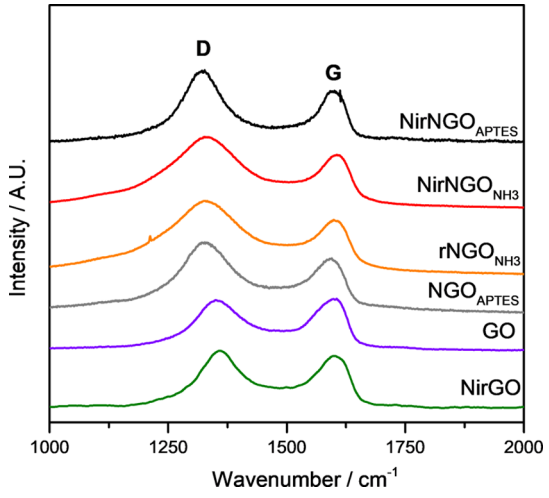

Figure 3. Raman spectra of freshly synthesized **Ni-NrGO$_{NH_3}$**, **Ni-NrGO$_{APTES}$**, **Ni-rGO**,[24] pristine GO, and nitrogenated GO (**NrGO$_{NH_3}$** and **NGO$_{APTES}$**) samples supported on a silicon wafer.

additives and Ni-rGO electrodes. The recording of spectra from different areas on the surface of each sample did not show significant differences.

All spectra from the electrodes surface show the GO characteristic bands, that is, G (first-order scattering of the E_{2g} phonon of sp^2 C atoms) and D signals (the defect-induced breathing mode of sp^2 rings, which arises from C−C bond stretching, and its intensity is related to the size of the in-plane sp^2 domains).[27] No spectroscopic signals from nickel oxide or another surface species were observed, which confirms the presence of GO particles incorporated in the structure of nickel electrodeposits.

Spectroscopic parameters from the nickel electrodeposited electrodes and individual components of the hybrids are presented in Table 2. The wavenumber from the D signal is

Table 2. Raman Parameters: D and G Peak Positions FMHW and the I_D/I_G Integrated Intensity Ratio

	D signal (cm^{-1})	G signal (cm^{-1})	FMHW$_D$ (cm^{-1})	FMHW$_G$ (cm^{-1})	I_D/I_G
Ni-NrGO$_{APTES}$	1327.2	1596.4	111.3	65.21	1.37
NGO$_{APTES}$	1327.2	1595.2	156.81	80.93	1.36
Ni-NrGO$_{NH_3}$	1327.7	1605.6	217.37	72.82	1.46
NrGO$_{NH_3}$	1325.3	1598.9	230.85	76.73	1.52
Ni-rGO	1357.4	1598.4	126.83	82.93	1.06
GO	1349.2	1598.1	148.02	80.37	0.95

practically constant at around 1327 cm^{-1} for all nitrogenated samples (particles and hybrids electrodes), with the exception of **Ni-rGO** and GO particles with D values at 1357 and 1349 cm^{-1}, respectively. It is clearly established that the presence of nitrogen atoms in the GO particles produces a downshift of the D band, compared with pristine GO flakes. Furthermore, the FWHM$_D$ is higher for ammonia-modified electrodes.

The downshift of the G band wavenumber in **Ni-NrGO$_{APTES}$** and **NGO$_{APTES}$** samples is a feature that can be associated with the doping concentration of the carbon network.[28] On the other side, it is known that the presence of N atoms in the GO structure produces increase of D′ band intensity at ca. 1605 cm^{-1},[29] which is the case of **Ni-NrGO$_{NH_3}$** catalysts.

All spectra of N-containing samples have values of the I_D/I_G ratio higher than the same species without nitrogen, and the increase of I_D/I_G and FWHM$_G$ values confirms that nitrogen groups can be incorporated in the hybrid material during the Ni electrodeposition process, being able to produce structural changes which cause larger relative disorder. Furthermore, the reduction of GO or NGO particles during the nickel electrodeposition process is also evidenced by the increase of I_D/I_G values. In fact, the observed increase of the I_D/I_G ratio can be attributed to the diminution in the size of in-plane sp^2 carbon domains because of the nitrogen incorporation of N in the flake and simultaneous electroreduction of GO. It means that the building higher amount of sp^2 carbon (graphite domains) compared with pristine GO flakes occurs during the Ni-hybrid conformation.[30,31]

DOI: 10.1021/acsomega.8b02895
ACS Omega 2019, 4, 2206−2216

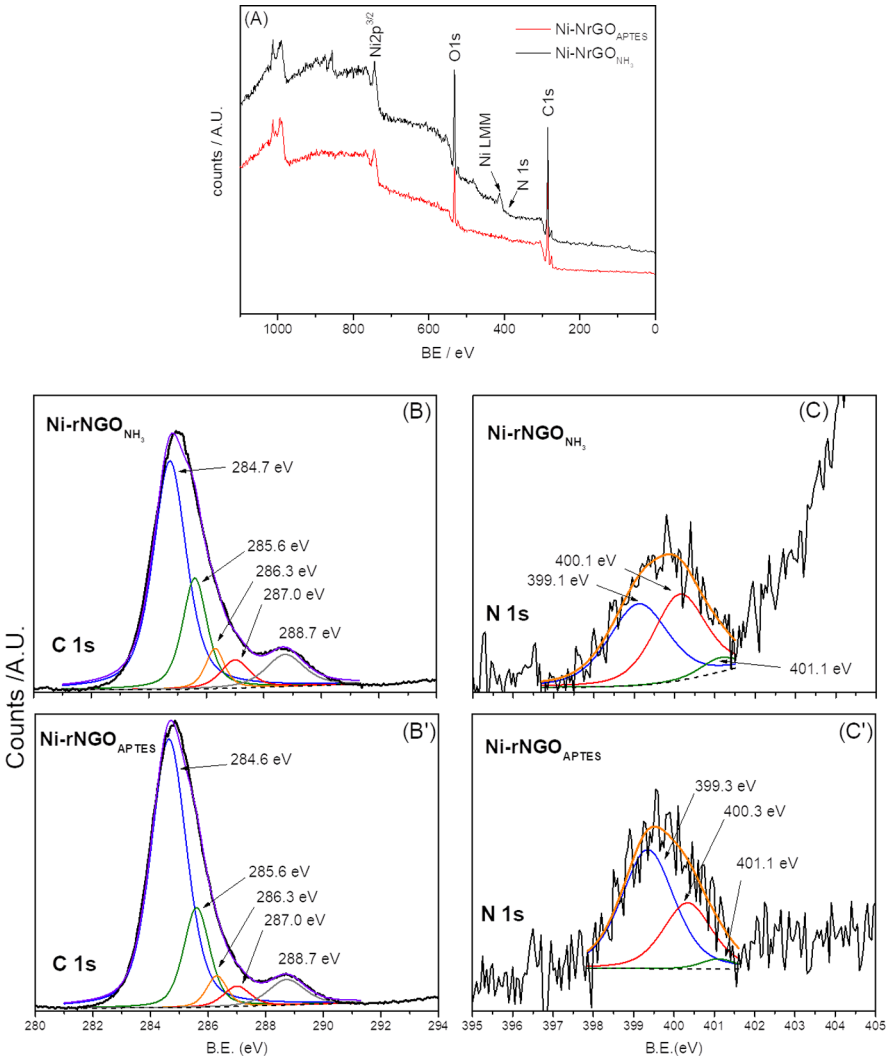

Figure 4. (A) Complete XPS spectra, (B,B′) C 1s zone, and (C,C′) N 1s zone for **Ni-NrGO$_{APTES}$** and **Ni-NrGO$_{NH_3}$** catalysts, respectively.

Table 3. Binding Energy of C 1s and N 1s regions in XPS Spectra for Ni-NrGO$_{APTES}$ and Ni-NrGO$_{NH_3}$ Catalysts[a]

	C 1s				N 1s		
	peak	region	FWHM (eV)	at. %	peak	region	at. %
Ni-NrGO$_{APTES}$	(C−C)	284.7	1.4	58	N-pyridinic	398.8	18.8
	(C−N)	285.6	1.0	20.8	N-pyrrolic	399.7	67.8
	(C−OH)	286.3	0.8	5.8	N-graphitic	400.8	13.4
	(O−C−O)	287	1.2	6.1			
	(O−C═O)	288.7	1.6	9.3			
Ni-NrGO$_{NH_3}$	(C−C)	284.6	1.45	67.0	N-pyridinic	398.5	2.8
	(C−N)	285.6	1.1	18.2	N-pyrrolic	399.3	54.8
	(C−OH)	286.3	0.8	4.5	N-graphitic	400.3	42.4
	(O−C−O)	287.0	1.1	3.8			
	(O−C═O)	288.7	1.5	6.5			

[a]at. % refers to perceptual atoms (N or C contents) present in different configurations.

The largest values of I_D/I_G ratios are from **Ni-NrGO$_{NH_3}$** and **NrGO$_{NH_3}$**, which are related to the amount of defects that are introduced in the GO structure by:

(i) Functionalization with ammonia

(ii) Chemical reduction of GO during the **NrGO** precursor synthesis, and

(iii) Electrochemical reduction of **NrGO** during nickel electrodeposition.

Surface elemental composition to reveal the presence of nitrogen atoms in the carbon network of GO particles in the nickel hybrids was established by X-ray photoelectron spectroscopy (XPS) measurements, and the configuration of C−N bonding was analyzed through the C 1s and N 1s spectra

DOI: 10.1021/acsomega.8b02895
ACS Omega 2019, 4, 2206−2216

region from both electrodes. Figure 4A shows the complete XPS spectra for **Ni-NrGO$_{NH_3}$** and **Ni-NrGO$_{APTES}$**, where changes provided by the nitrogen presence in the nickel electrodeposits are evident. Nickel in the metallic state is present on both the electrodes. In particular, the area of the O 1s peak is much higher in the **Ni-NrGO$_{NH_3}$** electrode compared with **Ni-NrGO$_{APTES}$**, possibly because of the presence of a greater amount of oxygenated defects in the reduced GO formed during the nitrogenation process. This finding is consistent with Raman analysis, where that sample presents an intensified D band.

The C 1s region in spectra (Figure 4B,C) of both electrodes is composed of four components assigned to the no-oxidized graphite carbon structure (284.8 eV), hydroxyl (286.3 eV), epoxide (287.0 eV), and carboxyl groups (288.4 eV), with the normal composition from GO species. However, in our case, the signal assigned to C−N binding at 285.6 eV has a noticeable contribution in **Ni-NrGO$_{NH_3}$** and **NrGO$_{NH_3}$** electrodes. Associated to this evidence, we note that the signal from epoxide binding (−C−O−C−) has negligible intensity. These results are in agreement with Zhi et al.,[22] indicating that APTES functionalization of GO particles occurs by amino terminal groups binding at the epoxide sites on the basal plane of the GO structure. The presence of the N 1s peak in Figure 4B′,C′ is the specific evidence about N-doping of GO particles, which form part of both nickel coatings. The high resolution spectra of the N 1s region show three types of functional groups such as N-pyridinic, N-pyrrolic, and N-graphitic at 398.3, 399.4, and 401.1 eV, respectively[19,32,33]

Data in Table 3 show that integrated intensities (at. %) from components of C 1s peaks are equivalent for both catalysts, which is consistent because the GO concentration in both plating baths is the same. The percentage of C or N atoms was established by calculus of the peak area for each N-type species. It is well known that the quaternary nitrogen (graphitic nitrogen) has a p-doping effect, while N pyridinic and N pyrrolic contribute to the increase of the Fermi level (E_f) and DOS of graphene.[34−36] Considering the distribution of N 1s components observed (Table 3 and Figure 4C,C′), **Ni-NrGO$_{APTES}$** catalysts have 18.79% of N pyridinic, whereas the respective value for **Ni-NrGO$_{NH_3}$** is only 2.83%. Furthermore, we note that both hybrid materials have the highest N content as N pyrrolic species.

From the literature, it has also been shown that N pyridinic structures are the main groups that participate on the enhancement of the electrocatalytic activity and energy storage efficiency.[37] On the other side, the high values of specific capacitance and stability of these hybrid materials indicate that they are suitable supercapacitors[33] because the improvement of electrical conductivity of N-doped graphene films is possible by the presence of N pyrrolic groups.[38] The N pyridinic groups are linked to a vacant defect because of the localized pair of electrons, and quaternary N groups are at dangling bonds of graphene.[39]

Catalytic Activity Analysis. *Cyclic Voltammetry with Freshly Synthesized Electrodes.* Figure 5 shows the potentiodynamic behavior of nickel Watts and the two **Ni-NrGO** synthesized catalysts recorded at 25 °C in 1.0 M KOH solution with a scan rate of 10 mV s^{-1}. Comparison of voltammetric cycles between **Ni-NrGO$_{APTES}$**, **Ni-NrGO$_{NH_3}$**, and **Ni** electrodes shows that the N-doped Ni catalysts have

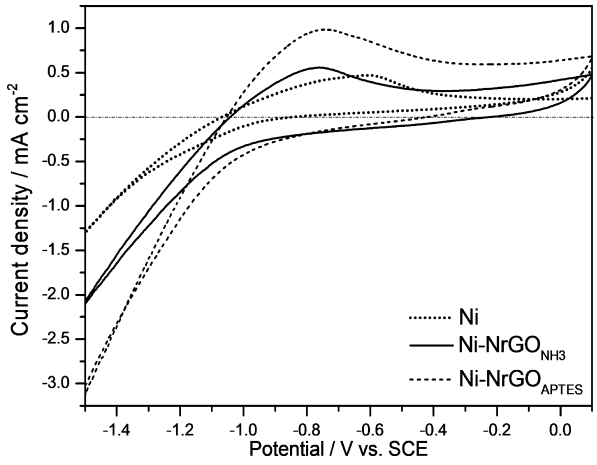

Figure 5. Cyclic voltammograms of fresh **Ni-NrGO$_{NH_3}$**, **Ni-NrGO$_{APTES}$**, and **Ni** electrodes in 1.0 M KOH at 25 °C at 10 mV s^{-1} scan rate.

the highest activity for HER. The current densities measured at −1.5 V (vs SCE) for **Ni-NrGO$_{APTES}$** and **Ni-rNGO$_{NH_3}$** are 2.35 and 1.62 times higher than those for Ni electrodes, respectively (Table 4). In both cases, the incorporation of nitrogen-rGO particles in the freshly synthesized **Ni-rGO** matrix results in an increment of the current density for HER. Similar behavior has been published for hybrid electrodes based on nickel and nitrogenated-carbon materials in acidic media.[40,41] Furthermore, the **Ni-NrGO$_{APTES}$** catalyst shows a decrease (50 mV) in the onset potential (OP) with respect to pure nickel electrodes, while **Ni-NrGO$_{NH_3}$** has OP values 100 mV higher.

The mechanism of the hydrogen generation in the alkaline electrolyte on nickel electrodes is based on the following three steps[42,43]

$$\mathrm{Ni} + \mathrm{H_2O} + \mathrm{e^-} \underset{k_{-V}}{\overset{k_V}{\rightleftharpoons}} \mathrm{Ni{\cdots}H_{ad}} + \mathrm{HO^-}\ \text{(Volmer reaction)}$$

$$2\mathrm{Ni{\cdots}H_{ad}} \underset{k_{-T}}{\overset{k_T}{\rightleftharpoons}} 2\mathrm{Ni} + \mathrm{H_2}\ \text{(Tafel reaction)}$$

$$\mathrm{Ni{\cdots}H_{ad}} + \mathrm{H_2O} + \mathrm{e^-} \underset{k_{-H}}{\overset{k_H}{\rightleftharpoons}} \mathrm{Ni} + \mathrm{HO^-} + \mathrm{H_2}\ \text{(Heyrovsky reaction)}$$

The steps in this mechanism are based on the adsorption and recombination of H atoms on the nickel nuclei to form H_2, so it considers nickel as the only catalyst of the reaction, while any additive in the structure of the hybrid electrode is taken as a modifying agent of the nickel band structure and not as part of the hydrogen generation reaction.[44]

Although each of the steps has a different Tafel slope associated, it is well known that Tafel slopes close to 120 mV dec^{-1} indicate that the Volmer electrode reaction with transference of one electron is the rate-determining step in the mechanism for HER.[45,46] The values calculated for Ni and **Ni-NrGO** electrodes presented in Table 4 are higher than expected for the Volmer reaction. This is probably due to the presence of coupled reactions such as the reduction of oxygenated groups in the GO structure.

Furthermore, increased catalytic activity of both NrGO-modified nickel electrodes is clearly evidenced by the exchange

DOI: 10.1021/acsomega.8b02895
ACS Omega 2019, 4, 2206−2216

Table 4. Electrochemical and Kinetic Parameters for HER on the Synthesized Catalysts Measured in 1.0 M KOH: Deactivation Rate (δ), Current Density (j), OP, Tafel Slope (b), and Exchange Current Density (j_0)

electrocatalysts	Ni	Ni-NrGO$_{APTES}$	Ni-NrGO$_{NH_3}$
$\delta/10^{-3}$ s^{-1}	1.95	1.85	1.47
$j_{at\ -1.5V\ (vs\ SCE)}$/mA cm^{-2}[a]	−1.30	−3.05	−2.10
$j_{at\ -1.5V\ (vs\ SCE)}$/mA cm^{-2}[b]	−1.30	−3.20	−1.53
OP/V (vs SCE)[a,b]	−1.00	−0.95	−1.10
b/V dec^{-1}[a]	−0.151	−0.162	−0.202
b/V dec^{-1}[b]	−0.147	−0.162	−0.141
j_0/mA cm^{-2}[a]	2.56 × 10^{-8}	2.53 × 10^{-5}	8.53 × 10^{-4}
j_0/mA cm^{-2}[b]	1.44 × 10^{-8}	2.53 × 10^{-5}	2.15 × 10^{-3}

[a]Fresh catalysts. [b]Aged catalysts.

current values, which are for **Ni-NrGO** electrodes, 3−4 orders higher than Ni catalysts according to the voltammetric analysis.

Chronoamperometry for Short Ageing Treatment. The freshly synthesized electrodes were subjected to a short ageing treatment to evaluate their stability during the hydrogen production. A chronoamperometric pulse at −1.5 V (vs SCE) in 1.0 M KOH solution was applied during 4 h at 25 °C. The treatment simultaneously involves a continuous rotation (at 900 rpm) of the electrode to remove the bubbles from the surface. Figure 6 shows the current density evolution of the

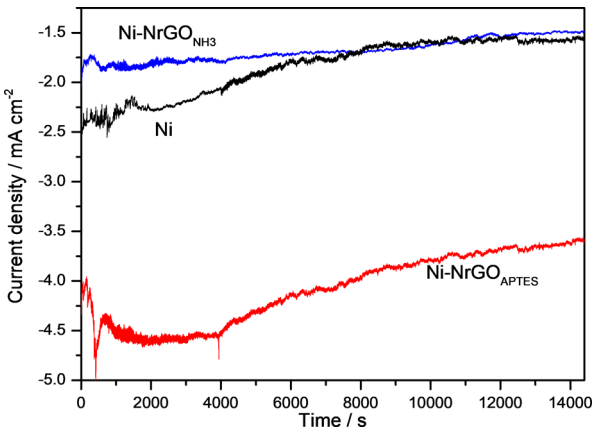

Figure 6. Chronoamperometric profiles from the ageing treatment of the catalysts, measured at −1.5 V (vs SCE) in 1.0 M KOH at 25 °C for 4 h.

catalysts during the ageing time. After 4 h, the current density decays to −1.56 A cm^{-2} for the pure Ni electrode, to −1.50 A cm^{-2} for **Ni-NrGO$_{NH_3}$**, and to −3.60 A cm^{-2} for **Ni-NrGO$_{APTES}$**, the latter being the catalyst that shows the best performance for hydrogen production, around 130% higher than Ni and **Ni-NrGO$_{NH_3}$**. The catalyst deactivation rate (δ) was calculated using eq 1[47]

$$\delta = -\frac{100}{j_e}\left(\frac{dj}{dt}\right) \quad (1)$$

where j_e is the extrapolated current density at the beginning of the polarization, and the dj/dt slope is evaluated from the linear decay at times higher to 4000 s (linear fit of the current profile). Both nitrogenated graphene electrodes present a lower deactivation rate than **Ni** (Table 4), and it is only 5% lower for **Ni-NrGO$_{APTES}$** and 25% for **Ni-NrGO$_{NH_3}$**. Therefore, the hybrid catalysts could have a longer useful half-life than pure nickel.

The differences in the trends found in the measurements of cyclic voltammetry and chronoamperometry are due to the fact that in cyclic voltammetry, each potential is swept for a very short time to analyze the processes that occur on the electrode, such as the generation of hydrogen, while in the chronoamperometric experiments, not only the fast processes can be detected but also the slow ones which are related to the ageing of the catalysts. For this reason, not necessarily, the trends observed in one of the techniques will remain valid in the other because they are analyzing temporarily different processes.[48,49]

Comparative analysis of the electrochemical characteristics (potentiodynamic behavior and electrical properties) of the hybrid material, before and after the continuous hydrogen production (ageing treatment), can be useful to understand the differences in their catalytic activity.

Characterization of Aged Electrodes. Table 4 also presents the electrochemical parameters obtained from voltammograms of Figure 7 for aged electrodes. We can observe that the OP for HER is the same as that for freshly synthesized electrodes.

For **Ni-NrGO$_{NH_3}$**, 27% lower current density is obtained after the ageing treatment, while for **Ni-NrGO$_{APTES}$**, 5% higher current density is found, indicating that the electrode undergoes a slight activation. Calculated Tafel slopes (Table 4) only present a significant change for the **Ni-NrGO$_{NH_3}$**,

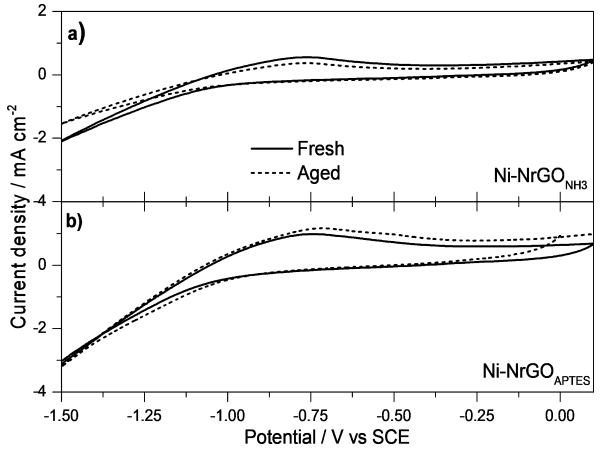

Figure 7. Cyclic voltammograms recorded at 25 °C and 10 mV s^{-1} scan rate recorded in 1.0 M KOH with (a) fresh (continuous line) and (b) aged (dashed lines) **Ni-NrGO$_{NH_3}$** and **Ni-NrGO$_{APTES}$** catalysts.

DOI: 10.1021/acsomega.8b02895
ACS Omega 2019, 4, 2206−2216

where the decrease in b that brings it closer to the value obtained for nickel Watts, is observed. The opposite effect can be observed in the exchange current for the **Ni-NrGO$_{NH_3}$** with an increase of 2.52 times. These results show that the catalytic activity for HER after ageing has the following order: **Ni-NrGO$_{APTES}$**^{a} > **Ni-NrGO$_{NH_3}$**^{a} ≥ **Ni**^{a} electrodes. Raman spectra are very useful to detect the presence of nickel hydroxide on the surface, whose formation can occur during ageing and often can be associated with the deactivation process of pure nickel electrodes.[24] In Figure 8, the absence of nickel hydroxides[50] and barely noticeable changes between fresh and aged synthesized electrodes indicate high stability of the material.

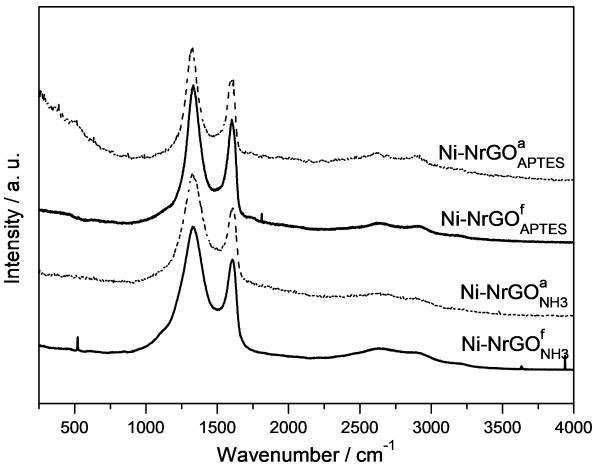

Figure 8. Raman spectra from fresh (continuous lines) and aged (dashed lines) **Ni-NrGO$_{APTES}$** and **Ni-NrGO$_{NH_3}$** catalysts.

Electrochemical Impedance Spectroscopy Analysis. Armstrong and Henderson have presented an equivalent circuit (denoted as AHEC) that can be used to fit impedance data for HER on nickel electrodes in alkaline medium.[51] This includes two semicircles in the complex plane of the Nyquist plot. For porous or very rough electrodes, there is usually observed in the complex plane remarkably flattened semicircles; for that reason, the addition of a constant phase element (CPE) in the circuit is necessary because of capacitance dispersion.[52,53] The AHEC model modified with a CPE (AHEC1CPE) describes a simple hydrogen evolution process, usually found on polycrystalline Ni and some Ni-based porous electrodes.[54,55]

In Figure 9A, the Nyquist curves for nickel nitrogenated graphene catalysts before and after ageing process, at 25 °C, are presented. Three potentials were selected to examine the behavior during the HER: E_1 = OP corresponding to each catalyst (−0.95 V_{SCE} for **Ni-NrGO$_{APTES}$** and −1.10 V_{SCE} for **Ni-NrGO$_{NH_3}$**), E_2 = (OP − 0.1) V, and E_3 = (OP − 0.3) V_{SCE}. At high frequency (HF) values, the semicircle observed is related to the surface geometry, whereas that recorded at low frequency (LF) can be referred to the charge-transfer process. The behavior at HF is independent of the overpotential applied but that at LF shows a strong dependence of this variable.[53] On the other side, the decrease of the semicircle diameters in the area of LF when the overpotential increases indicates that the charge-transfer resistance decreases. Therefore, the catalytic activity is higher and the production of hydrogen is greater.

In this work, several equivalent circuits which are shown in Figure 9[56] were employed to fit the experimental data. In the first place, the well-known Randles (Rand) and modified Randles with CPE (RandCPE) models were tested. However, a better fit of spectra was obtained with the conventional AHEC, the modified AHEC with one or two CPE (AHEC1CPE and AHEC2CPE, respectively), and with a model containing 2 CPE in series (2CPE).[57] In those equivalent circuits, R1 represents the solution resistance, C1 (in some cases replaced by CPE1) means the electric double layer capacitor, R2 represents the charge-transfer resistance, and CPE2 together with R3 are related to the pores and surface roughness.

Considering χ^2 as a setting parameter with values lower than 0.01, a very good approximation to the experimental data was obtained with AHEC1CPE, AHEC2CPE, 2CPE, and RandCPE for both **Ni-NrGO** catalysts. It is important to clarify that the Randles−CPE model only adjusts the first semicircle, unlike the other models derived from the Armstrong and Henderson model.

Table 5 shows the fitting parameters obtained for electrocatalysts at 0.1 V from OP potential and compares the models AHEC2CPE with RandCPE to evidence the difference between a circuit that can describe the phenomena in the HER reaction, with one that has the limitations described before. Taking into account the AHEC2CPE model, the R2 (related with the charge-transference) increases for the **Ni-NrGO$_{NH_3}$** after the ageing process, but for **Ni-NrGO$_{APTES}$**, this parameter shows a decrease. This feature is in accordance with the potentiodynamic behavior in Figure 7, where the current density for the ammonium-based electrode decreases showing deactivation, and the APTES-based electrodes seem to show the opposite effect.

CONCLUSIONS

In this work, nitrogenated graphene−nickel electrodes for HER, synthesized under two different configurations, are presented.

Silanization of GO with APTES molecules allows the incorporation of particles to the nickel coating, promoting the construction of **Ni-NrGO$_{APTES}$** electrodes with better efficiency for hydrogen production. This means achieving 130% higher current density than **Ni-NrGO$_{NH_3}$** or pure nickel electrodes. Another advantage shown is the simplicity of the method to manufacture these catalysts because it is possible to incorporate the nitrogen-GO particles by making a slight modification to the Watts bath. The **Ni-NrGO$_{NH_3}$** electrodes show a good behavior for HER, but the synthesis with heating and pressurization steps in the hydrothermal method is more complex.

We have shown that both NGO particles contain incorporated pyrrolic nitrogen in the graphene structure, but **Ni-NrGO$_{NH_3}$** electrodes also have graphitic nitrogen. Because both the surface roughness as well as the crystal size and the proportions of crystalline active planes are similar, the difference in the catalytic activity can be explained on the basis of N-doping with the incorporated rGO particles, which also affects the structure of the catalysts. The **Ni-NrGO$_{APTES}$** electrode shows a lower OP for HER, which results in superior hydrogen production with lower energy consumption.

DOI: 10.1021/acsomega.8b02895
ACS Omega 2019, 4, 2206−2216

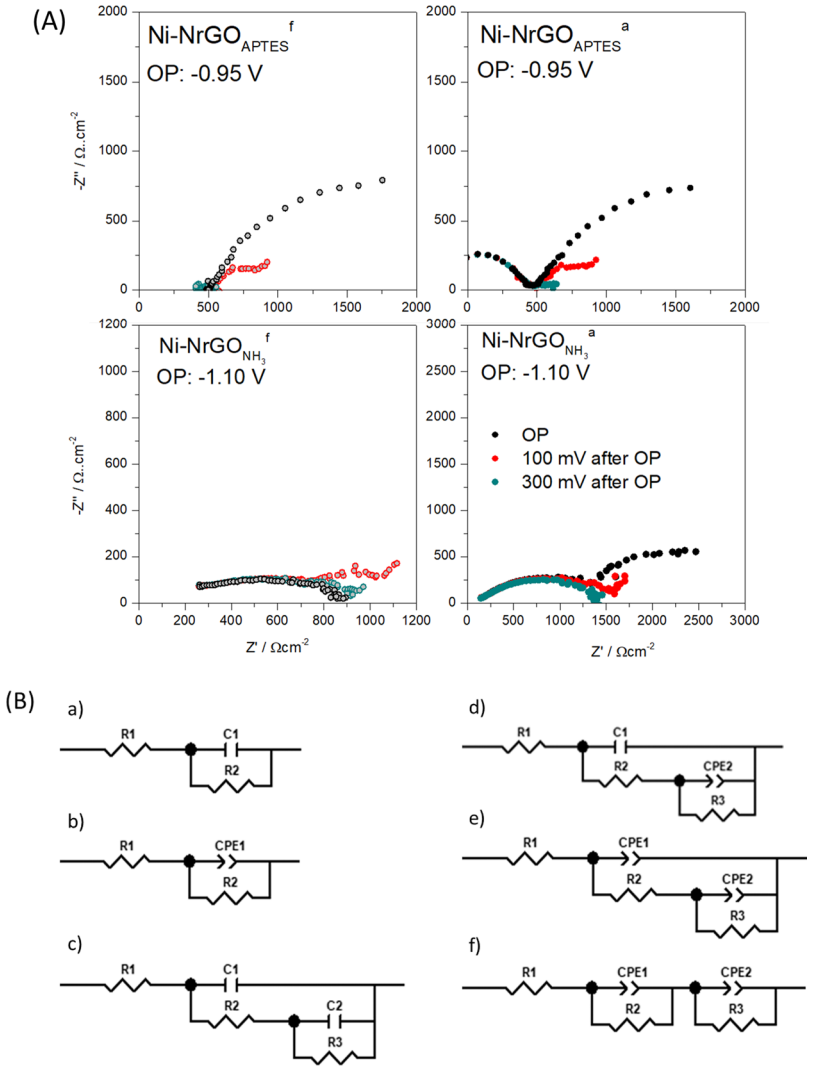

Figure 9. (A) Nyquist plots at OP, 0.1 and 0.3 V after OP at 25 °C for "fresh" and "aged" electrodes. (B) Fitting models for equivalent circuits used for electrochemical impedance spectroscopy (EIS). (a) Rand, (b) RandCPE, (c) AHEC, (d) AHEC1CPE, (e) AHEC2CPE, and (f) 2CPE.

Table 5. Experimental Electrical Components Obtained from Fit the Data (Figure 9A) with the AHEC2CPE and RandCPE Circuits (Figure 9B), for Fresh and Aged Electrodes at 0.1 V More Cathodic Than OP

circuit elem.	Ni-NrGO$_{NH_3}$ ^{f}	Ni-NrGO$_{NH_3}$ ^{a}	Ni-NrGO$_{APTES}$ ^{f}	Ni-NrGO$_{APTES}$ ^{a}
AHEC2CPE				
R1	17.19	15.97	99.3	19.87
R2	34.23	319.1	102.6	68.49
CPE1	7.70×10^{-5}	2.53×10^{-4}	3.35×10^{-3}	7.95×10^{-7}
CPE2	8.59×10^{-4}	4.9×10^{-2}	4.64×10^{-2}	5.59×10^{-3}
R3	154.8	2476	382.4	187.7
RandCPE				
R1	16.5	14.87	98.99	92.66
R2	190.4	326.2	115.2	142.5
CPE1	6.49×10^{-4}	2.71×10^{-4}	3.89×10^{-3}	4.62×10^{-3}

Raman measurements have evidenced the absence of nickel hydrides and nickel hydroxides at **Ni-NrGO** electrodes, species that are responsible for deactivation of pure nickel electrocatalysts. This is reflected in the lower deactivation rates obtained during the ageing process. Considering these characteristics, we can resume that **Ni-NrGO$_{APTES}$** is a better alternative than pure electrodeposited nickel, analyzed in a long-term use because it has a higher hydrogen production with a promising longer half-life.

EXPERIMENTAL SECTION

Chemicals and Reagents. Nickel sulfate (Anedra, PA grade), nickel chloride (Merck, PA grade), boric acid (Merck, PA grade), ethanol 96% (Cicarelli, PA grade), hydrochloric acid 36.5−37% (Cicarelli, PA grade), potassium hydroxide (Anedra RA reagent) APTES 99% (Sigma-Aldrich), ammonium hydroxide 28−30% (J.T. Baker), and GO dispersion (Graphenea Inc.) were used as received. All solutions were prepared with Milli-Q water and degassed employing high purity N_2 (Indura S.A.).

Graphene Nitrogenation. N-GO particles were synthesized by two different methods. The "ammonium method" involves a hydrothermal process to obtain NrGO. For this purpose, 80 mL of ammonium hydroxide solution (30% w/w) was added to 20 mL of 0.08 g/L GO dispersion under stirring for 1 h at 40 °C and then sonicated for 30 min. The aqueous dispersion was settled in an autoclave for the hydrothermal reaction at 220 °C during 24 h. In this step, the GO flakes were doped with nitrogen and simultaneously reduced to rGO. The

DOI: 10.1021/acsomega.8b02895
ACS Omega 2019, 4, 2206−2216

final product was centrifuged to collect the nanomaterial $\mathbf{NrGO_{NH_3}}$.[20]

The second method is the silanization of GO with APTES. In this case, 0.1 mL of APTES−toluene solution (1% v/v) was added to 10 mL of 0.08 g/L GO dispersion at room temperature and intensively stirred for 10 min. Residual APTES and toluene were thoroughly rinsed with toluene and water for its removal, leaving GO particles functionalized with APTES ($\mathbf{NGO_{APTES}}$) in solution. This process is based on the direct reaction of the APTES precursor with hydroxyl groups on the carbon skeleton.[58] Moreover, Xi et al. have shown that the amine group of APTES reacts with epoxide groups from GO; therefore, a moiety of GO could be considered as reduced.[22]

Both forms of hybrid particles contain nitrogen in different structural configurations. **N-rGO** particles have the nitrogen atoms incorporated on the carbon positions in the planar mesh, while amino groups from APTES are included as functional external groups.

Electrodeposition of Nickel-Based Hybrids. A conventional Watts bath for nickel plating was prepared by dissolution in water of 25 g of boric acid (at 50 °C), 240 g of nickel sulfate hexahydrate, and 25 g of nickel chloride hexahydrate. In order to prepare $\mathbf{Ni\text{-}NrGO_{NH_3}}$ catalysts, 10 mL of 0.08 g L^{-1} $\mathbf{NrGO_{NH_3}}$ dispersion was added to 40 mL of the Watts bath. For $\mathbf{Ni\text{-}NrGO_{APTES}}$ catalysts, the $\mathbf{NGO_{APTES}}$ dispersion was sonicated for 30 min to separate the NGO flakes, and then 10 mL of $\mathbf{NGO_{APTES}}$ was added to 40 mL of Watts bath.

The synthesis of both catalysts was carried out by electrodeposition on a Ni polycrystalline electrode (RC S.A. 99.9 purity), with 0.196 cm^2 of exposed circular area, which is mounted on a rotating disk electrode support (Pine Research Inst.; Raleigh, NC). The nickel electrodes were polished with 0.05 μm alumina, cleaned with ethanol, and pretreated with consecutive immersion steps in KOH (1 M) and HCl (10% w/w) solutions in order to clean the surface. Electrodeposition of both catalysts were carried out in a two-electrode electrochemical cell, thermostated at 50 °C using a massive nickel counter electrode with a high surface area. During the process, the homogeneity of the electrodeposits was controlled maintaining the working electrode at a rotation rate of 1600 rpm.

The current density applied during the synthesis was −0.05 A cm^{-2} for 1800 s in order to obtain a deposit thickness of around 30 μm. During the electrodeposition of both catalysts, the potential-time transient reached a value of around −5.0 V, which indicates that the codeposited GO flakes should be in a reduced state condition where the graphene is highly conductive.[59] After the synthesis, the electrodes were washed repeatedly with Milli-Q water in order to remove the remainder of the plating bath from the electrode surface.

Catalysts Characterization. SEM images were taken with a Supra 40 FE-SEM Sigma (Zeiss Company) with an acceleration voltage of 5 kV and filament current of 10 mA.

Raman spectra of the electrode surface were acquired with a LABRAM-HR 800, HORIBA Jobin-Yvon Raman microscope with a 100× objective lens (NA = 0.9). The laser excitation used was 633 nm at 3.5 mW. The instrument allows recording spectra with a resolution of 1.5 cm^{-1}. The illuminated area in all Raman experiments was 1.0 μm^2. At least five different zones on each sample were analyzed to confirm the homogeneity of the catalysts.

X-ray diffractograms were measured using λ = 1.5406 Å Cu Kα radiation employing a PANalytical X'Pert PRO diffractometer operating at 40 kV and 40 mA, in the $\theta-2\theta$ Bragg−Brentano geometry. All measurements were carried out at room temperature. The 2θ range used was 10−70°, with 0.02° steps and counting time of 2 s per step. The Rietveld method was used to refine the crystal structure employing the FullProf program.[60] A pseudo-Voigt shape function was used to fit the experimental data. The data refined were lattice parameters, atomic positions, isotropic thermal parameters, peak shape, and occupation factors.

The XPS analysis was performed in a Multitechnique Specs system with a dual X-ray source (Mg/Al) and a hemi-spherical analyzer PHOIBOS 150 in the fixed analyzer transmission mode. The spectra were recorded with 30 eV step energy, with Mg anode. The working power was 80 W. The pressure during the measurement was less than 2×10^{-8} mbar. The electrodes were subjected to ultrahigh vacuum for at least 12 h before measurements. The XPS spectra analysis was carried out using the XPS peak 4.1 fitting program.

Confocal microscopy images were obtained using Olympus LEXT OLS4000, employing a 405 nm wavelength laser, magnifications of 1070× and 2132×, with a pitch in the z axis of 0.05 and 0.01 μm with areas for data collection of (258 μm)^2 and (130 μm)^2, respectively. Data from confocal microscopy images were employed to determine rms values of the surfaces.

Electrocatalytic Activity Studies. Evaluation of the electrocatalytic activity with synthesized electrodes was performed by recording the voltammetric current for HER in 1 M KOH. The experiments were carried out in a three-electrode electrochemical cell equipped with a thermostatic jacket. During the entire electrochemical measurements, a high purity N_2 flux was maintained over the electrolyte surface to deoxygenate the solution. A large area platinum foil was used as the counter electrode and a saturated calomel electrode (SCE) as the reference electrode (0.243 V vs RHE). The temperature of the electrochemical cell was 25 °C using a Lauda Alpha RA 8 controller. On the other hand, the reference electrode was kept at room temperature by maintaining it out of the electrochemical cell and the circuit was closed using a Luggin capillary.

An Autolab PGStat30 potentiostat/galvanostat coupled to a FRA2 module was employed. The uncompensated ohmic drop correction was conducted as presented elsewhere.[57] The area used for all current densities calculation was 0.196 cm^2 (the geometric area of the disk electrode). The potential was scanned between 0.1 and −1.5 V (vs SCE) at a scan rate of 10 $mV{\cdot}s^{-1}$ for all electrodes. EIS analysis of the catalysts was performed in the frequency range between 10 mHz and 100 kHz with a 10 mV bias potential. EIS was recorded at different electrode potentials: E_1 (open circuit potential, OCP), E_2 (HER, OP), E_3, and E_4 (100 and 300 mV more cathodic than the corresponding OP of each catalyst, respectively), in order to cover the potential range where the HER occurs. The ZView 3.3 software (Scribner Associates, Inc.) was used for data fit with the equivalent circuit models.

Analysis of electrodes stability was performed keeping them in continuous hydrogen production by applying a potential pulse of −1.5 V (vs SCE) during 4 h at 298 K in 1 M KOH. The chronoamperometric profiles were recorded in order to study the surface changes after the short ageing process. A 900 rpm electrode rotation rate was used for EIS and

DOI: 10.1021/acsomega.8b02895
ACS Omega 2019, 4, 2206−2216

chronoamperometric experiments. This is to prevent blocking of surface sites with hydrogen bubbles.

AUTHOR INFORMATION

Corresponding Authors

*E-mail: estebanfranceschini@yahoo.com.ar. Fax: 54 0351 433 4188 (E.A.F.).

*E-mail: glacconi@fcq.unc.edu.ar (G.I.L.).

ORCID

Gabriela I. Lacconi: 0000-0002-9518-7343

Notes

The authors declare no competing financial interest.

REFERENCES

(1) Panchakarla, L. S.; Subrahmanyam, K. S.; Saha, S. K.; Govindaraj, A.; Krishnamurthy, H. R.; Waghmare, U. V.; Rao, C. N. R. Synthesis, structure, and properties of boron- and nitrogen-doped graphene. *Adv. Mater.* **2009**, *21*, 4726−4730.

(2) Ju, H.; Badwal, S.; Giddey, S. A comprehensive review of carbon and hydrocarbon assisted water electrolysis for hydrogen production. *Appl. Energy* **2018**, *231*, 502−533.

(3) Lavorante, M. J.; Franco, J. I. Performance of stainless steel 316L electrodes with modified surface to be use in alkaline water electrolyzers. *Int. J. Hydrogen Energy* **2016**, *41*, 9731−9737.

(4) Kuckshinrichs, W.; Koj, J. C. Levelized cost of energy from private and social perspectives: The case of improved alkaline water electrolysis. *J. Cleaner Prod.* **2018**, *203*, 619−632.

(5) Saba, S. M.; Müller, M.; Robinius, M.; Stolten, D. The investment costs of electrolysis - A comparison of cost studies from the past 30 years. *Int. J. Hydrogen Energy* **2018**, *43*, 1209−1223.

(6) Schalenbach, M.; Tjarks, G.; Carmo, M.; Lueke, W.; Mueller, M.; Stolten, D. Acidic or Alkaline? Towards a New Perspective on the Efficiency of Water Electrolysis. *J. Electrochem. Soc.* **2016**, *163*, F3197−F3208.

(7) Wang, M.; Wang, Z.; Gong, X.; Guo, Z. The intensification technologies to water electrolysis for hydrogen production - A review. *Renewable Sustainable Energy Rev.* **2014**, *29*, 573−588.

(8) Geim, A. K.; Novoselov, K. S. The rise of graphene. *Nat. Mater.* **2007**, *6*, 183−191.

(9) Shaari, N.; Kamarudin, S. K. Graphene in electrocatalyst and proton conductiong membrane in fuel cell applications: An overview. *Renewable Sustainable Energy Rev.* **2017**, *69*, 862−870.

(10) Seetharaman, S.; Balaji, R.; Ramya, K.; Dhathathreyan, K. S.; Velan, M. Graphene oxide modified non-noble metal electrode for alkaline anion exchange membrane water electrolyzers. *Int. J. Hydrogen Energy* **2013**, *38*, 14934−14942.

(11) Ahmad, H.; Fan, M.; Hui, D. Graphene oxide incorporated functional materials: A review. *Composites, Part B* **2018**, *145*, 270−280.

(12) Kaur, M.; Kaur, M.; Sharma, V. K. Nitrogen-doped graphene and graphene quantum dots: A review onsynthesis and applications in energy, sensors and environment. *Adv. Colloid Interface Sci.* **2018**, *259*, 44−64.

(13) Derycke, V.; Martel, R.; Appenzeller, J.; Avouris, P. Controlling doping and carrier injection in carbon nanotube transistors. *Appl. Phys. Lett.* **2002**, *80*, 2773−2775.

(14) Gong, K.; Du, F.; Xia, Z.; Durstock, M.; Dai, L. Nitrogen-doped carbon nanotube arrays with high electrocatalytic activity for oxygen reduction. *Science* **2009**, *323*, 760−764.

(15) Wang, S.; Wang, X.; Jiang, S. P. PtRu nanoparticles supported on 1-aminopyrene-functionalized multiwalled carbon nanotubes and their electrocatalytic activity for methanol oxidation. *Langmuir* **2008**, *24*, 10505−10512.

(16) Wang, S.; Yang, F.; Jiang, S. P.; Chen, S.; Wang, X. Tuning the electrocatalytic activity of Pt nanoparticles on carbon nanotubes via surface functionalization. *Electrochem. Commun.* **2010**, *12*, 1646−1649.

(17) Ewels, C. P.; Glerup, M. Nitrogen doping in carbon nanotubes. *J. Nanosci. Nanotechnol.* **2005**, *5*, 1345−1363.

(18) Du, L.; Luo, L.; Feng, Z.; Engelhard, M.; Xie, X.; Han, B.; Sun, J.; Zhang, J.; Yin, G.; Wang, C.; Wang, Y.; Shao, Y. Nitrogen-doped graphitized carbon shell encapsulated NiFe nanoparticles: A highly durable oxygen evolution catalyst. *Nano Energy* **2017**, *39*, 245−252.

(19) Yadav, R.; Dixit, C. K. Synthesis, characterization and prospective applications of nitrogen-doped graphene: A short review. *J. Sci. Adv. Mater. Dev.* **2017**, *2*, 141−149.

(20) Liang, Y.; Li, Y.; Wang, H.; Zhou, J.; Wang, J.; Regier, T.; Dai, H. Co3O4 nanocrystals on graphene as a synergistic catalyst for oxygen reduction reaction. *Nat. Mater.* **2011**, *10*, 780−786.

(21) Zheng, D.; Vashist, S. K.; Al-Rubeaan, K.; Luong, J. H. T.; Sheu, F.-S. Mediatorless amperometric glucose biosensing using 3-aminopropyltriethoxysilane-functionalized graphene. *Talanta* **2012**, *99*, 22−28.

(22) Zhi, X.; Mao, Y.; Yu, Z.; Wen, S.; Li, Y.; Zhang, L.; Chan, T. W.; Liu, L. γ-Aminopropyl triethoxysilane functionalized graphene oxide for composites with high dielectric constant and low dielectric loss. *Composites, Part A* **2015**, *76*, 194−202.

(23) Zhuang, Z.; Giles, S. A.; Zheng, J.; Jenness, G. R.; Caratzoulas, S.; Vlachos, D. G.; Yan, Y. Nickel supported on nitrogen-doped carbon nanotubes as hydrogen oxidation reaction catalyst in alkaline electrolyte. *Nat. Commun.* **2016**, *7*, 10141−10148.

(24) Franceschini, E. A.; Lacconi, G. I. Synthesis and Performance of Nickel/Reduced Graphene Oxide Hybrid for Hydrogen Evolution Reaction. *Electrocatalysis* **2018**, *9*, 47−58.

(25) Dahal, A.; Batzill, M. Graphene-nickel interfaces: a review. *Nanoscale* **2014**, *6*, 2548−2562.

(26) Yu, Q.; Zhou, T.; Jiang, Y.; Yan, X.; An, Z.; Wang, X.; Zhang, D.; Ono, T. Preparation of graphene-enhanced nickel-phosphorus composite films by ultrasonic-assisted electroless plating. *Appl. Surf. Sci.* **2018**, *435*, 617−625.

(27) Ferrari, A. C.; Robertson, J. Interpretation of Raman spectra of disordered and amorphous carbon. *Phys. Rev. B: Condens. Matter Mater. Phys.* **2000**, *61*, 14095−14107.

(28) Das, A.; Pisana, S.; Chakraborty, B.; Piscanec, S.; Saha, S. K.; Waghmare, U. V.; Novoselov, K. S.; Krishnamurthy, H. R.; Geim, A. K.; Ferrari, A. C.; Sood, A. K. Monitoring dopants by Raman scattering in an electrochemically top-gated graphene transistor. *Nat. Nanotechnol.* **2008**, *3*, 210−215.

(29) Zafar, Z.; Ni, Z. H.; Wu, X.; Shi, Z. X.; Nan, H. Y.; Bai, J.; Sun, L. T. Evolution of Raman spectra in nitrogen doped graphene. *Carbon* **2013**, *61*, 57−62.

(30) Tuinstra, F.; Koenig, J. L. Raman spectrum of graphite. *J. Chem. Phys.* **1970**, *53*, 1126−1130.

(31) Loh, K. P.; Bao, Q.; Eda, G.; Chhowalla, M. Graphene oxide as a chemically tunable platform for optical applications. *Nat. Chem.* **2010**, *2*, 1015−1024.

(32) Zhang, L.-S.; Liang, X.-Q.; Song, W.-G.; Wu, Z.-Y. Identification of the nitrogen species on N-doped graphene layers and Pt/NG composite catalyst for direct methanol fuel cell. *Phys. Chem. Chem. Phys.* **2010**, *12*, 12055−12059.

(33) Xu, H.; Ma, L.; Jin, Z. Nitrogen-doped graphene: Synthesis, characterizations and energy applications. *J. Energy Chem.* **2018**, *27*, 146−160.

(34) Chen, M.; Wang, L.; Yang, H.; Zhao, S.; Xu, H.; Wu, G. Nanocarbon/oxide composite catalysts for bifunctional oxygen reduction and evolution in reversible alkaline fuel cells: A mini review. *J. Power Sources* **2018**, *375*, 277−290.

(35) Panchakarla, L. S.; Subrahmanyam, K. S.; Saha, S. K.; Govindaraj, A.; Krishnamurthy, H. R.; Waghmare, U. V.; Rao, C. N. R. Synthesis, structure, and properties of boron- and nitrogen-doped graphene. *Adv. Mater.* **2009**, *21*, 4726−4730.

(36) Biel, B.; Blase, X.; Triozon, F.; Roche, S. Anomalous doping effects on charge transport in graphene nanoribbons. *Phys. Rev. Lett.* **2009**, *102*, 096803−0968034.

DOI: 10.1021/acsomega.8b02895
ACS Omega 2019, 4, 2206−2216

(37) Cho, Y. J.; Kim, H. S.; Baik, S. Y.; Myung, Y.; Jung, C. S.; Kim, C. H.; Park, J.; Kang, H. S. Selective Nitrogen-Doping Structure of Nanosize Graphitic Layers. *J. Phys. Chem. C* **2011**, *115*, 3737−3744.
(38) Lee, D. H.; Lee, W. J.; Kim, S. O.; Kim, Y.-H. Theory, synthesis, and oxygen reduction catalysis of Fe-porphyrin-like carbon nanotube. *Phys. Rev. Lett.* **2011**, *106*, 175502−1755024.
(39) Hwang, J. O.; Park, J. S.; Choi, D. S.; Kim, J. Y.; Lee, S. H.; Lee, K. E.; Kim, Y.-H.; Song, M. H.; Yoo, S.; Kim, S. O. Workfunction-Tunable, N-Doped Reduced Graphene Transparent Electrodes for High-Performance Polymer Light-Emitting Diodes. *ACS Nano* **2012**, *6*, 159−167.
(40) Pan, Y.; Yang, N.; Chen, Y.; Lin, Y.; Li, Y.; Liu, Y.; Liu, C. Nickel phosphide nanoparticles-nitrogen-doped graphene hybrid as an efficient catalyst for enhanced hydrogen evolution activity. *J. Power Sources* **2015**, *297*, 45−52.
(41) Wang, S.; Wang, J.; Zhu, M.; Bao, X.; Xiao, B.; Su, D.; Li, H.; Wang, Y. Molybdenum-Carbide-Modified Nitrogen-Doped Carbon Vesicle Encapsulating Nickel Nanoparticles: A Highly Efficient, Low-Cost Catalyst for Hydrogen Evolution Reaction. *J. Am. Chem. Soc.* **2015**, *137*, 15753−15759.
(42) Losiewicz, B.; Budniok, A.; Rowinski, E.; Lagiewka, E.; Lasia, A. The structure, morphology and electrochemical impedance study of the hydrogen evolution reaction on the modified nickel electrodes. *Int. J. Hydrogen Energy* **2004**, *29*, 145−157.
(43) Harrington, D. A.; Conway, B. E. ac Impedance of Faradaic reactions involving electrosorbed intermediates-I. Kinetic theory. *Electrochim. Acta* **1987**, *32*, 1703−1712.
(44) Sharma, L.; Khushwaha, H. S.; Mathur, A.; Halder, A. Role of molybdenum in Ni-MoO 2 catalysts supported on reduced graphene oxide for temperature dependent hydrogen evolution reaction. *J. Solid State Chem.* **2018**, *265*, 208−217.
(45) Franceschini, E. A.; Lacconi, G. I.; Corti, H. R. Kinetics of the hydrogen evolution on nickel in alkaline solution: New insight from rotating disk electrode and impedance spectroscopy analysis. *Electrochim. Acta* **2015**, *159*, 210−218.
(46) Mahmood, N.; Yao, Y.; Zhang, J. W.; Pan, L.; Zhang, X.; Zou, J.-J. Electrocatalysts for Hydrogen Evolution in Alkaline Electrolytes: Mechanisms, Challenges, and Prospective Solutions. *Adv. Sci.* **2018**, *5*, 1700464.
(47) Franceschini, E. A.; Lacconi, G. I.; Corti, H. R. Hydrogen evolution kinetics on Ni cathodes modified by spontaneous deposition of Ag or Cu. *J. Energy Chem.* **2017**, *26*, 466−475.
(48) Facci, P. Useful Notions in Electrochemistry. *Biomolecular Electronics Bioelectronics and the Electrical Control of Biological Systems and Reactions Micro and Nano Technologies*; Elsevier Science, 2014; Chapter 2, pp 19−47.
(49) Pletcher, D.; Greff, R.; Peat, R.; Peter, L. M.; Robinson, R. *Instrumental Methods in Electrochemistry*; Woodhead Publishing, 2010.
(50) Hall, D. S.; Lockwood, D. J.; Poirier, S.; Bock, C.; MacDougall, B. R. Raman and Infrared Spectroscopy of α and β Phases of Thin Nickel Hydroxide Films Electrochemically Formed on Nickel. *J. Phys. Chem. A* **2012**, *116*, 6771−6784.
(51) Armstrong, R.; Henderson, M. Impedance Plane Display of a Reaction with an Adsorbed Intermediate. *J. Electroanal. Chem. Interfacial Electrochem.* **1972**, *39*, 81−90.
(52) de Levie, R. On the impedance of electrodes with rough interfaces. *J. Electroanal. Chem.* **1989**, *261*, 1−9.
(53) Hitz, C.; Lasia, A. Experimental study and modeling of impedance of the her on porous Ni electrodes. *J. Electroanal. Chem.* **2001**, *500*, 213−222.
(54) Lasia, A.; Rami, A. Kinetics of hydrogen evolution on nickel electrodes. *J. Electroanal. Chem.* **1990**, *294*, 123−141.
(55) Gomez, M. J.; Franceschini, E. A.; Lacconi, G. I. Ni and NixCoy Alloys Electrodeposited on Stainless Steel AISI 316L for Hydrogen Evolution Reaction. *Electrocatalysis* **2018**, *9*, 459−470.
(56) Daftsis, E.; Pagalos, N.; Jannakoudakis, A.; Jannakoudakis, P.; Theodoridou, E.; Rashkov, R.; Loukaytsheva, M.; Atanassov, N. Preparation of a Carbon Fiber-Nickel-Type Material and Investigation of the Electrocatalytic Activity for the Hydrogen Evolution Reaction. *J. Electrochem. Soc.* **2003**, *150*, C787−C793.
(57) Franceschini, E. A.; Lacconi, G. I.; Corti, H. R. Kinetics of hydrogen evolution reaction on nickel modified by spontaneous Ru deposition: A rotating disk electrode and impedance spectroscopy approach. *Int. J. Hydrogen Energy* **2016**, *41*, 3326−3338.
(58) Pérez, L. A.; Klug, J.; Coronado, E. A.; Lacconi, G. I. Chemical and Electrochemical Oxidation of Silicon Surfaces Functionalized with APTES: The Role of Surface Roughness in the AuNPs Anchoring Kinetics. *J. Phys. Chem. C* **2013**, *117*, 11317−11327.
(59) Sobon, G.; Sotor, J.; Jagiello, J.; Kozinski, R.; Zdrojek, M.; Holdynski, M.; Paletko, P.; Boguslawski, J.; Lipinska, L.; Abramski, K. M. Graphene Oxide vs Reduced Graphene Oxide as saturable absorbers for Er-doped passively mode-locked fiber laser. *Opt. Express* **2012**, *20*, 19463−19473.
(60) Rodríguez-Carvajal, J. Recent advances in magnetic structure determination by neutron powder diffraction. *Phys. B* **1993**, *192*, 55−69.

DOI: 10.1021/acsomega.8b02895
ACS Omega 2019, 4, 2206−2216